Application of a meta-analysis of aortic geometry to the generation of a compliant phantom for use in particle image velocimetry experimentation

Larissa Huetter*. Patrick H. Geoghegan. Paul D. Docherty**.**
Milad Soltanipour Lazarjan. Don Clucas**. Mark Jermy**.**

**Karlsruhe Institute of Technology, Karlsruhe, Germany,*
(Tel: 0049 176 973 49275; e-mail: larissa.huetter@student.kit.edu).
*** Department of Mechanical Engineering, University of Canterbury, Christchurch, New Zealand*
(e-mail: patrick.geoghegan@canterbury.ac.nz, paul.docherty@canterbury.ac.nz,
milad.soltanipourlazarjan@pg.canterbury.ac.nz,
don.clucas@canterbury.ac.nz, mark.jermy@canterbury.ac.nz)

The evolution of pressure-flow geometry in the aortic arch is increasingly understood as a key element in the treatment of hemodynamic dysfunction in patients. However, little is known about the properties of the flow across the aortic geometry and thus the sensitivity of sensor placement is also unknown. Compliant models of the aortic path can be built to allow techniques such as particle image velocimetry to measure the velocity fields.

This paper presents the justification and production methodology used to generate a compliant model of the aortic arch that represents the geometry and compliance of typical hemodynamics patients. The information from twenty papers was synthesized to generate a single model of the aortic arch. The model incorporates the three branching arteries at an apex of a tapering aortic path experimental that has been manufactured as a flexible thin-walled silicon model. Calculations were undertaken to ensure that the model matches the *in vivo* compliance of the arteries.

The experimental setup uses the compliant silicone model of the aorta with variable flow pump to mimic the cardiac cycle, and a variable extramural pressure to mimic changes in intrathoracic pressure. This research was necessary for the development of an accurate experimental setup that would enable results that are immediately applicable to the research of cardiovascular therapy optimization.

Keywords: Aortic Arch, Compliant Vessels, Windkessel model, Blood flow, Particle Image Velocimetry (PIV).

1. INTRODUCTION

Cardiovascular diseases are the most common cause of mortality. The World Health Organisation (2015)estimates that 17.5 million people died in 2012 as a result of a disease in the heart or supplying blood vessel. Hemodynamic dysfunction accounts for a significant fraction of ICU admissions and is comparatively intense to treat (Dickstein 2005; Roger *et al.* 2011). Treatment is often supplemented with inotrope and fluid resuscitation. However, both treatments have risks that can exacerbate the patient state (Durairaj and Schmidt 2008; Rivers *et al.* 2010).

The aorta is the biggest blood vessel in the human body. The ascending aorta is connected to the left chamber of the heart. It is followed by the aortic arch with the three branching arteries: the brachiocephalic, which carries blood to the right arm and the head, the left common carotid which is responsible for the blood flow to the head, and the left subclavian artery that is connected to the left arm. The descending aorta carries the blood to the lower part of the body.

During systole, the heart pushes blood via left ventricular contraction into the aorta. The increased aortic pressure causes the diameter of the ascending aorta to increase to 120-160% of the end diastolic diameter. The discontinuous flow of the heart becomes a more constant flow in the aorta due to the compliance of the artery walls. This effect, which reduces the pulse-pressure in the blood circuit, is called the Windkessel effect (Kamoi *et al.* 2014; Manning *et al.* 2002).

During systole, the critical Reynolds number is exceeded in the proximal aorta. This causes a temporary turbulent flow field. Turbulent flow can also be found when blood velocity increases due to diseases like vascular stenosis or anemia, which causes a reduction in blood viscosity (Schmidt *et al.* 2011). The complex flow dynamics in this process have been the subject of many papers over the last decades (Arzani *et al.* 2012; Benim *et al.* 2011; Gülan *et al.* 2012; Kim *et al.* 2004; Laumen *et al.* 2010; Shahcheraghi *et al.* 2002; Vasava *et al.* 2010). However, these studies were typically based on rigid vessels. Having the right compliance (flexibility) in the arterial wall, is one of the challenges that must be overcome to fully mimic the fluid-structure interaction (FSI). Failing to incorporate artery compliance significantly reduces the

accuracy of the model (Geoghegan *et al.* 2013) and limits the potential benefit of such studies.

This work compiles and reports geometric data of the aortic arch taken from twenty articles from scientific literature. From this data, an idealized elastic phantom of the aortic arch suitable for optical measurements was generated. The experimental setup to analyze the fluid dynamics in the arch via particle image velocimetry (PIV) is presented in this paper.

2. LITERATURE RESEARCH

2.1 Aortic geometry

Table 1 presents geometric data of the ascending aorta, the aortic arch and the descending aorta, as well as those of the three arteries branching at the apex of the aortic arch. Fig. 3 labels each of the parts presented in Table 1. Only the geometries of young healthy people were considered to provide geometries for a generalized person without any abnormalities.

Table 1. Geometries of the Aorta (ascending, descending and aortic arch) and branching arteries (brachiocephalic, left common carotid and left subclavian artery) taken from Vasava *et al.* (2010), Redheuil *et al.* (2011), Avolio (1980).

	Geometry
Ascending Aorta	Length 18-40 mm Radius 12.5- 14.5 mm Wall-thickness 1.63 mm
Aortic Arch	Length 59-100.4 mm Radius 10.7-11.2 mm Wall-thickness 1.27-1.32 mm Curvature 0.034 mm^{-1} Width 58.6 mm Height 34.3 mm
Descending Aorta	Length 139.3 - 156 mm Radius 9.15-12.5 mm Wall-thickness 1.16-1.2 mm
Brachiocephalic Artery	Length 28-34 mm Radius 4.25-6,2 mm Wall-Thickness 0.86 mm
Left Common Carotid Artery	Length 28-89 mm Radius 3.7-4.25 mm Wall-Thickness 0.63 mm
Left Subclavian Artery	Length 28-34 mm Radius 4.2-4.95 mm Wall-Thickness 0.67 mm

Caballero and Laín (2013) provides a review on the progress of computational fluid dynamics (CFD) modelling of blood flow in the aortic arch. The paper provides the model building technique and presents equations which govern replication of the vessel distensibility reproduction in the phantom. It also compares the assumptions regarding material properties and boundary conditions. It was found that computational simulations provide information on the development and origin of some cardiovascular diseases. However, current studies contribute more toward disease understanding rather than etiological monitoring or optimisation algorithms for therapy. Caballero and Laín (2013) claimed that the greatest benefit form aortic flow modelling will be achieved when patient-specific characterization of fluid behaviour with patient-specific boundary conditions is undertaken. This challenge requires patient-specific phantoms and could potentially be used to predict the outcomes of specific therapeutic choices and thus, optimise therapy.

There is significant inter-patient variance in aortic geometry. However, some dependence has been observed according to gender and age (Redheuil *et al.* 2011). In particular, the aortic diameter increases an average of 7 mm over 50 years. The aortic arch diameter tends to be larger closest to the heart and transitions to a smaller diameter as it approaches the descending aorta. The aortic wall thickness is also largest near the heart (Avolio 1980; Wang and Parker 2004). A reason for the stiffness in this region might be the high pulse pressure between systole and diastole. Table 2 shows some of the key properties of the aortic arch and the range of characteristics that might be encountered by a typical individual.

Table 2: Boundary conditions of the aorta (Avolio 1980; Ntsinjana *et al.* 2013; Redheuil *et al.* 2011; Schmidt *et al.* 2011).

Distensibility	7-120 $kPa^{-1}x10^{-3}$
Young's Modulus	0.4-1.071 x 10^6 N/m^2
Cardiac Output	5.6 l/min
Systolic Blood Pressure	113-173 mmHg
Diastolic Blood Pressure	68-80 mmHg
Peak Heart Rate	162- 188 bpm

2.2 Flow field visualisation techniques

Some investigations of blood flow used both rigid and compliant phantoms for optical measurements. In addition, investigations have also used computational models of the aortic arch (Benim *et al.* 2011; Kim *et al.* 2004; Shahcheraghi *et al.* 2002). Benim *et al.* (2011) used a rigid CFD model of aortic flow. Bertoglio *et al.* (2013) used a FSI model. With the latter, they showed that they could use the algorithm directly in a real clinical case. However, they reported that future work should include the interaction of the aorta with surrounding tissues, fluid field measurements and improvement of the geometries.

Phantom studies generate physical representations of the geometry of interest and generate a flow field which are measured in a variety of ways. The flow field may not necessarily use the same type of working fluid, however, good experimental setups will ensure that common Reynolds and Womersley numbers are used (Geoghegan *et al.* 2012). Rapid prototyping a mould and casting silicone is an option (Biglino *et al.* 2013; Geoghegan *et al.* 2012). For the printing

process idealised geometry can be produced from data in literature or patient-specific CT or MRI scans can be used to generate highly accurate moulds that are representative of the patient. Geoghegan *et al.* (2012) describes a technique using Dow Corning Sylgard 184 silicone (E= $1{,}32*10^6$ N/m^2) to fabricate bubble free flow phantoms with both rigid as well as compliant walls. The silicone has a refractive index of 1.415-1.47. This matches the refractive index of a 39/61 water-glycerol mixture. The mixture has a density of 1,140 kg/m^3 and a viscosity of 1.06 x 10^{-2} Pa at 20°C. In comparison, blood has a density of 1,060 kg/m^3 and a viscosity of around 3.5 x 10^{-3} Pa at body temperature. Reynolds matching was applied to ensure dynamic similarity between blood and the water/glycerol mixture. In the previous study by (Geoghegan *et al.* 2012), plaster was used to print the female mould. Plaster could be dissolved easily with water, leaving the silicone phantom geometry. However, high precision 3D printed plaster has been superseded by 3D printing of ABS materials and thus plaster printers are not widely available. 3D printed plaster is also more fragile than ABS plastic and is more susceptible to failure during the moulding process.

Flow field capture can be undertaken via particle tracking velocimetry (Gülan *et al.* 2012). However, PIV is the most common method (Geoghegan *et al.* 2012; Kaufmann *et al.* 2014; Laumen *et al.* 2010; Pielhop *et al.* 2014; Pielhop *et al.* 2014). Pielhop *et al.* (2014) studied an elastic curved vessel without any branching arteries and a homogenous wall thickness of 1 mm. The model was fabricated using a two component polydimethylsiloxane (RTV 15) with a Young's Modulus of $1.24*10^6$ N/m^2.

Biglino *et al.* (2013) studied the compliance of TangoPlus (Stratasys 2014) using rapid prototyping of a small section of the descending aorta with different wall-thickness and printing methods. However, the material was found to be too rigid for accurate representation of the distensibility of the artery wall. Zürcher (2003) used experimentally derived outcomes using laser-Doppler anemometer as boundary conditions for a computational model of pulsatile flow in the aortic arch. The phantom models included elastic and rigid models of the aortic arch and arteries. The silicone (Wacker SilGel601) had a Young's Modulus of $1.9*10^6$ N/m^2 and a refractive index of 1.413. However, in this study, the tissue pressure was neglected.

3. MODEL CONSTRUCTION

The distensibility in the model varies between $17*10^{-6}$ and $32*10^{-6}$ m^2/N across the model geometry. The actual geometries and the results of the calculation can be seen in Table 3.

The phantom construction technique to be used in this analysis is a development of the method presented by Geoghegan *et al.* (2012). The aortic phantom is an idealized model constructed from the geometric data provided in Table 1. The model consists of the ascending and descending aorta, the aortic arch, the brachiocephalic, the left common carotid and the left subclavian artery (Fig. 3). It has been assumed that all vessels could be effectively modelled using a material that has a consistent Young's Modulus. To make the compliance of the silicone phantom match *in vivo* conditions, the distensibility of the artery and those of the model must match. Hence, match *in vivo* distensibility conditions, the model wall thickness was modulated.

$$\left(\frac{1}{E\left(\frac{h}{D}\right)}\right)_{model} = \left(\frac{1}{E\left(\frac{h}{D}\right)}\right)_{artery}$$

where E is the Young's Modulus, h is the wall-thickness, D is the internal diameter of the vessel. All arteries are axisymmetric and the xy-plane is the symmetric plane.

Table 3 Geometric Data of the Model, Young's Modulus E [N/m2 x106], Wall-Thickness h [mm], Diameter D [mm]

		Aortic Arch	Des-cending Aorta	Brachio-cephalic Artery	Left Common Carotid Artery	Left Sub-clavian Artery
Data Artery	E	0.526	0.526	0.700	0.700	0.700
	H	1.32	1.2	0.86	0.63	0.67
	D	22	20	12.4	7.4	8.4
Data Model 1:1	E	1.320	1.320	1.320	1.320	1.320
	H	0.658	0.438	0.324	0.384	0.419
	D	27.5	18.3	8.8	8.5	9.9
Model 1:1	H	0.66	0.44	0.32	0.38	0.42
Model 1:1.5	H	0.99	0.66	0.48	0.57	0.63

To allow for more robust fabrication, the geometry was scaled up by 50%. As the wall thickness of the thinnest part of the scaled model is just 0.48 mm, a test model was produced to assess the viability of the technique to generate such thin sections.

To build the silicone phantom, the internal mould was constructed in SolidWorks using values from the geometric data from table 1. The model was printed on a Stratasys Dimension Elite 3D printer with ABS plastic. After the model was cured for 48 hours, an acetone bath (Munro *et al.* 2014) was used to smooth the surface of the model that was rough due to the layering process of the 3D printer. In this study, only healthy younger people had been taken into consideration. However, it has been noted that there are significant changes in the geometries of the aortic diameter and the arch length with age (Redheuil *et al.* 2011).

The fidelity of the printed model with respect to the original CAD model was investigated using an Artec Spider 3D scanner. Fig. 1 shows that the maximal deviation between the model and the print data is 0.4 mm. If the external mould was constructed in ignorance of this deviation from the assumed internal mould, it would have resulted in a minimum wall thickness of approximately 0.08mm. This would cause a considerable discrepancy in the distensibility of the artery.

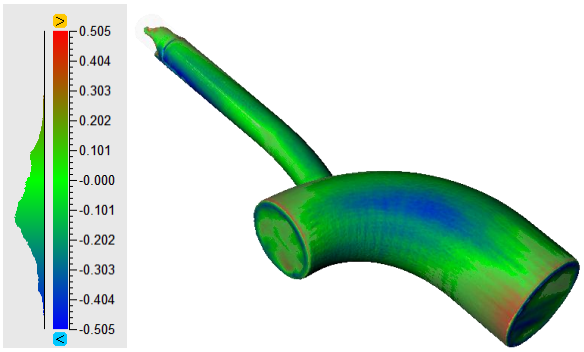

Fig. 1 Variation in mm between printed, smoothed internal model and CAD file.

Fig. 2 Test mould with the internal mould (blue) placed in the external mould (grey)

To achieve a homogenous wall-thickness of 0.48 mm in the brachiocephalic artery Geometric Design X was used to construct the external mould using the scan data. The external mould (Fig. 2) was CNC machined in Ebalta S-Modelboard and coated with enamel spray paint. The spray paint achieved a smooth surface and stopped perfusion of the silicone into the mould during the curing process. To construct the phantom, silicone was injected into the bottom cavity inlet close to the brachiocephalic artery (Fig. 2). This ensured that no air gaps are formed due to flow effects. This method was used in accordance with previous successful mould making exercises (Geoghegan *et al.* 2012). In total the material costs for the phantom was ~$380(NZD); 3D printing cost ~$160, the external mould ~ $150 and the silicone cost ~$70. For the full aortic model (Fig. 3), due to printer size restrictions, a three part model was constructed and glued together.

4. EXPERIMENTAL SETUP

The compliant silicone model will be used for an analysis of the blood flow via PIV. PIV is a contact-free measurement technique, which uses two cameras for three dimensional visualization of the flow field. The silicone phantom is submersed in a working fluid of comparable refractive index. The working fluid inside the phantom is impregnated with tracer particles that are illuminated with a pulsed laser and captured via cameras that take pairs of pictures (at t and t+dt)

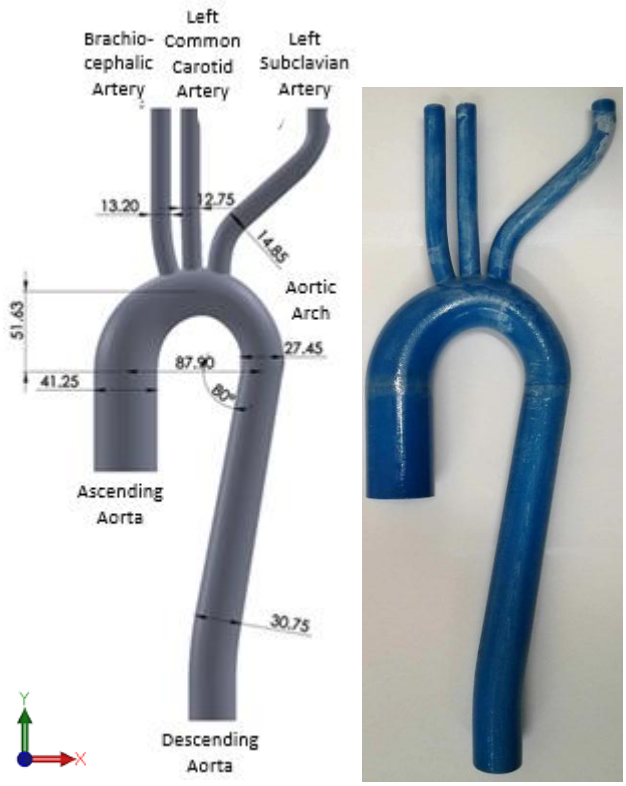

Fig. 3 1:1.5 Model of the aorta with its geometries solid modelled (left) and the printed plastic model after smoothing (right)

(Raffel *et al.* 2007). The particles are tracked between images and flow filed velocities can be calculated.

To enable PIV analysis of pulsatile flow within the compliant phantom geometry, the phantom will be placed in a pressure box (Fig. 4) that is connected to a pump system producing a physiologically realistic cardiac flow wave (Geoghegan *et al.* 2013) that includes mimicry of the aortic valve closing. At each end of the model, a silicone end plate connects the phantom to the box. These rigid connections restrict the longitudinal compliance of the model and support the flow field in a physiological manner. The back pressures in the arteries as well as the outer pressure in the pressure box are adjustable. This experimental setup allows the modelling of a range of healthy and dysfunctional hemodynamic states.

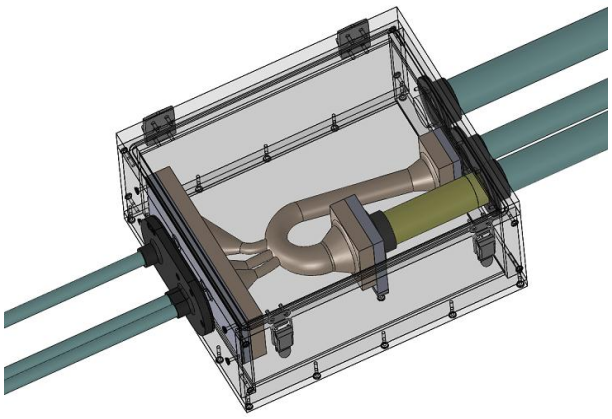

Fig. 4 : Model in pressure box with connecting pipes.

The pressure box is connected to a flow system (Fig. 5). Five header tanks with weirs control the back pressure in the arteries and of the descending aorta as well as the tank pressure. The header tanks height is variable and thus different boundary conditions can be mimicked. In particular, modulation of the tank pressure will be used to mimic changes in inter-thoracic pressure.

5. DISCUSSION

In this research we have generated a model of a representative aortic geometry that can be used in an experiment to determine the pressure flow field characteristics of the human aorta. This could yield important information to guide further research into the hemodynamic therapy for critically ill patients, predict the performance of surrogate heart valves *in silico*, or model the outcomes of coronary artery disease. By ensuring that the geometry of the

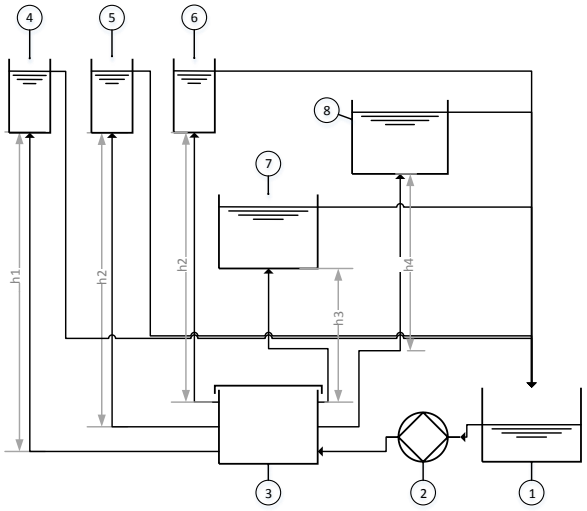

Fig. 5: Schematically experimental Setup. (1) overflow box and reservoir, (2) pump mimics cardiac emptying, (3) pressure box with model, (4-6) back pressure regulator boxes for brachiocephalic (4), left common carotid (5), left subclavian artery (6), (7) regulator box for tissue pressure, (8) back pressure box for descending aorta

aorta phantom is as close as possible to realistic conditions, this will increase the fidelity of the results. However, the realism also required that a complex geometry is constructed with specific elastic properties.

In this analysis we have chosen to use additive manufacture rather than subtractive manufacturing process for the internal surface. This is due in part to the benefit of the additive manufacturing material being dissolvable after moulding the silicone. 3D printing allows better modelling of complex surfaces with cheaper and faster manufacturing.

However, the 3D printed internal mould was not a precise representation of the SolidWorks model of the aorta. There was settling of the material which caused the model to deviate up to 0.4 mm from the desired geometry. To overcome this problem, a 3D scanner was used to create a solid model of the printed geometry. This model was then used as a basis for the external mould that was CNC machined from Ebalta S-Modelboard material.

The geometry of the aortic arch depends on gender, age, central blood pressure and hemodynamic health of the individual (Redheuil *et al.* 2011). Therefore, a further step for this research is to consider the geometry of individuals that have hemodynamic dysfunction. To do this, access to MRI or CT data from the critically ill individuals to build a physiologically realistic model is required. The critically ill patient specific flow field could then be compared to the idealised one to measure the validity of some of the assumptions regarding hemodynamic dysfunction.

Furthermore, a range of phantoms that represent different stages on the pathogenesis of cardiovascular disease age groups could be created to investigate the role of the changing of the blood flow patterns in cardiovascular diseases.

6. CONCLUSION

This paper provides the geometric data and the necessary process to make a range of phantoms of the aortic arch. A method to fabricate a thin-walled compliant model with a variable wall-thickness across different sections of the aorta is presented. This compliant phantom of the aortic arch and surrounding geometries allows a realistic simulation of the flow field. In the experimental setup, the tissue pressure is considered and varied. This model is unique amongst existing models as it can match the Reynolds number of aortic flow, the Womersley number, the aortic compliance and also the intrathoracic pressure and the outlet pressure and resistance.

REFERENCES

Arzani A., Dyverfeldt P., Ebbers T., Shadden S.C. (2012) In vivo validation of numerical prediction for turbulence intensity in an aortic coarctation, *Ann Biomed Eng*, 40(4), 860-870

Avolio A. (1980) Multi-branched model of the human arterial system, *Medical and Biological Engineering and Computing*, 18(6), 709-718

Benim A.C., Nahavandi A., Assmann A., Schubert D., Feindt P., Suh S.H. (2011) Simulation of blood flow in human aorta with emphasis on outlet boundary conditions, *Applied Mathematical Modelling*, 35(7), 3175-3188

Bertoglio C., Barber D., Gaddum N., Valverde I., Rutten M., Beerbaum P., Moireau P., Hose R., Gerbeau J.F. (2013) Identification of artery wall stiffness: in vitro validation and in vivo results of a data assimilation procedure applied to a 3D fluid-structure interaction model, *J Biomech*, 47(5), 1027-1034

Biglino G., Verschueren P., Zegels R., Taylor A.M., Schievano S. (2013) Rapid prototyping compliant arterial phantoms for in-vitro studies and device testing, *J Cardiovasc Magn Reson*, 15(2), 1-7

Caballero A.D., Laín S. (2013) A Review on Computational Fluid Dynamics Modelling in Human Thoracic Aorta, *Cardiovascular Engineering and Technology*, 4(2), 103-130

Dickstein K. (2005) Diagnosis and assessment of the heart failure patient: the cornerstone of effective management, *European journal of heart failure*, 7(3), 303-308

Durairaj L., Schmidt G.A. (2008) Fluid Therapy in Resuscitated Sepsis*Less Is More, *CHEST Journal*, 133(1), 252-263

Geoghegan P., Buchmann N., Soria J., Jermy M. (2013) Time-resolved PIV measurements of the flow field in a stenosed, compliant arterial model, *Experiments in fluids*, 54(5), 1-19

Geoghegan P., Buchmann N., Spence C., Moore S., Jermy M. (2012) Fabrication of rigid and flexible refractive-index-matched flow phantoms for flow visualisation and optical flow measurements, *Experiments in fluids*, 52(5), 1331-1347

Gülan U., Lüthi B., Holzner M., Liberzon A., Tsinober A., Kinzelbach W. (2012) Experimental study of aortic flow in the ascending aorta via Particle Tracking Velocimetry, *Experiments in Fluids*, 53(5), 1469-1485

Kamoi S., Pretty C., Docherty P.D., Squire D., Revie J., Chiew Y.S., Desaive T., Shaw G.M., Chase J.G. (2014) Continuous Stroke Volume Estimation from Aortic Pressure Using Zero Dimensional Cardiovascular Model: Proof of Concept Study from Porcine Experiments, *PLoS ONE*, 9(7), e102476

Kaufmann T.A., Neidlin M., Busen M., Sonntag S.J., Steinseifer U. (2014) Implementation of intrinsic lumped parameter modeling into computational fluid dynamics studies of cardiopulmonary bypass, *J Biomech*, 47(3), 729-735

Kim T., Cheer A.Y., Dwyer H.A. (2004) A simulated dye method for flow visualization with a computational model for blood flow, *Journal of Biomechanics*, 37(8), 1125-1136

Laumen M., Kaufmann T., Timms D., Schlanstein P., Jansen S., Gregory S., Wong K.C., Schmitz-Rode T., Steinseifer U. (2010) Flow analysis of ventricular assist device inflow and outflow cannula positioning using a naturally shaped ventricle and aortic branch, *Artif Organs*, 34(10), 798-806

Manning T.S., Shykoff B.E., Izzo J.L. (2002) Validity and Reliability of Diastolic Pulse Contour Analysis (Windkessel Model) in Humans, *Hypertension*, 39(5), 963-968

Munro B., Becker S., Uth M.F., Preußer N., Herwig H. (2014) Fabrication and Characterization of Deformable Porous Matrices with Controlled Pore Characteristics, *Transport in Porous Media*, 1-16

Ntsinjana H., Bigliono G., Capelli C., Giardini A., Derrick G., Schievano S., Taylor A.M. (2013) Abnormalities in aortic arch germetry do not lead to reduced exercise performance: a comparison study between patients with transposition of the great arteries repaired by arterial switch operation and normal controls, *Journal of Cardiovascular Magnetic Resonance*,

Pielhop K., Schmidt C., Zholtovski S., Klaas M., Schröder W. (2014) Experimental investigation of the flow field in an elastic 180 curved vessel,

Pielhop K., Schmidt C., Zholtovski S., Klaas M., Schröder W. (2014) Experimental investigation of the fluid–structure interaction in an elastic 180° curved vessel at laminar oscillating flow, *Experiments in Fluids*, 55(10), 1-13

Raffel M., Willert C., Wereley S., Kompenhans J. (2007) Particle image velocimetry: a practical guide second edition, *Springer (Berlin and New York)*,

Redheuil A., Yu W.-C., Mousseaux E., Harouni A.A., Kachenoura N., Wu C.O., Bluemke D., Lima J.A.C. (2011) Age-Related Changes in Aortic Arch Geometry: Relationship with Proximal Aortic Function and Left Ventricular Mass and Remodeling, *Journal of the American College of Cardiology*, 58(12), 1262-1270

Rivers E.P., Jaehne A.K., Eichhorn-Wharry L., Brown S., Amponsah D. (2010) Fluid therapy in septic shock, *Current Opinion in Critical Care*, 16(4), 297-308

Roger V.L., Go A.S., Lloyd-Jones D.M., Adams R.J., Berry J.D., Brown T.M., Carnethon M.R., Dai S., de Simone G., Ford E.S., Fox C.S., Fullerton H.J., Gillespie C., Greenlund K.J., Hailpern S.M., Heit J.A., Ho P.M., Howard V.J., Kissela B.M., Kittner S.J., Lackland D.T., Lichtman J.H., Lisabeth L.D., Makuc D.M., Marcus G.M., Marelli A., Matchar D.B., McDermott M.M., Meigs J.B., Moy C.S., Mozaffarian D., Mussolino M.E., Nichol G., Paynter N.P., Rosamond W.D., Sorlie P.D., Stafford R.S., Turan T.N., Turner M.B., Wong N.D., Wylie-Rosett J. (2011) Heart disease and stroke statistics--2011 update: a report from the American Heart Association, *Circulation*, 123(4), e18-e209

Schmidt R.F., Lang F., Heckmann M.: *Physiologie des Menschen: mit Pathophysiologie*. Springer-Verlag, 2011

Shahcheraghi N., Dwyer H., Cheer A., Barakat A., Rutaganira T. (2002) Unsteady and three-dimensional simulation of blood flow in the human aortic arch, *Transactions of the ASME*, 124(378-387

Stratasys: PolyJet Materials Data Sheet. 2014

Vasava P., Jalali P., Dabagh M.: Computational Study of Pulstile Blood Flow in Aortic Arch: Effect of Blood Pressure. In *World Congress on Medical Physics and Biomedical Engineering, September 7-12, 2009, Munich, Germany*, Springer, 2010, p. 1198-1201

Wang J., Parker K. (2004) Wave propagation in a model of the arterial circulation, *Journal of biomechanics*, 37(4), 457-470

World Health Organisation: Cardiovascular Diseases (CVDs), Fact Sheet No. 317. World Health Organisation, 2015

Zürcher L.: Simulation der Strömung in der menschlichen Aorta. Karlsruhe, Univ., Diss., 2003, 2003